Title

Towards assessing and improving the reliability of ultrashort echo time quantitative magnetization transfer (UTE-qMT) MRI of cortical bone: In silico and ex vivo study

Journal

Magnetic Resonance Materials in Physics, Biology and Medicine, 37(6)

ISSN

0968-5243

Authors

Shin, Soo Hyun

Moazamian, Dina

Tang, Qingbo

et al.

Publication Date

2024-08-10

DOI

10.1007/s10334-024-01190-7

Peer reviewed

Magnetic Resonance Materials in Physics, Biology and Medicine (2024) 37:983–992
https://doi.org/10.1007/s10334-024-01190-7

RESEARCH ARTICLE

Towards assessing and improving the reliability of ultrashort echo time quantitative magnetization transfer (UTE-qMT) MRI of cortical bone: In silico and ex vivo study

Soo Hyun Shin[1] · Dina Moazamian[1] · Qingbo Tang[2] · Saeed Jerban[1] · Yajun Ma[1] · Jiang Du[1,2,3] · Eric Y. Chang[1,2]

Received: 12 April 2024 / Revised: 5 July 2024 / Accepted: 8 July 2024 / Published online: 10 August 2024

Abstract

Objective To assess and improve the reliability of the ultrashort echo time quantitative magnetization transfer (UTE-qMT) modeling of the cortical bone.

Materials and Methods Simulation-based digital phantoms were created that mimic the UTE-qMT properties of cortical bones. A wide range of SNR from 25 to 200 was simulated by adding different levels of noise to the synthesized MT-weighted images to assess the effect of SNR on UTE-qMT fitting results. Tensor-based denoising algorithm was applied to improve the fitting results. These results from digital phantom studies were validated via ex vivo rat leg bone scans.

Results The selection of initial points for nonlinear fitting and the number of data points tested for qMT analysis have minimal effect on the fitting result. Magnetization exchange rate measurements are highly dependent on the SNR of raw images, which can be substantially improved with an appropriate denoising algorithm that gives similar fitting results from the raw images with an 8-fold higher SNR.

Discussion The digital phantom approach enables the assessment of the reliability of bone UTE-qMT fitting by providing the known ground truth. These findings can be utilized for optimizing the data acquisition and analysis pipeline for UTE-qMT imaging of cortical bones.

Keywords Ultrashort echo time (UTE) · Quantitative magnetization transfer (qMT) · MRI · Cortical bone · Digital phantom

Introduction

Bone fractures are a growing public health issue posing a serious worldwide healthcare and economic burden [1]. The risk of bone fractures is significantly increased in people with osteoporosis and diabetes, with the global prevalence of each disease estimated to be 19.7% [2] and 10.5% [3], respectively. The most widely used fracture risk assessment is dual-energy X-ray absorptiometry (DXA)-based bone mineral density (BMD) measurement. However, clinical studies have reported that the BMD measurement only explains 30–50% of fractures [4–6]. This limited sensitivity of BMD has motivated the need for more reliable fracture risk assessment tools that focus on not only the BMD but also other features and constituents of the bone, such as bone microstructure [7] and organic matrix [8, 9].

Magnetic resonance imaging (MRI) can not only provide anatomical images but also quantitative information on molecular components of tissues, leveraging its numerous contrast mechanisms. Quantitative magnetization transfer (qMT) imaging is one of the widely studied MRI methods for probing the macromolecular content and their properties in tissues [10–12]. While the usage of qMT imaging has been limited to soft tissues [13–17] (e.g., brain, muscle, spinal cord and kidney) due to the very short T_2* relaxation of hard tissues, combining qMT with an ultrashort echo time

✉ Soo Hyun Shin
shs033@health.ucsd.edu

✉ Eric Y. Chang
ericchangmd@gmail.com

[1] Department of Radiology, University of California San Diego, 9452 Medical Center Drive, La Jolla, CA, USA

[2] Radiology Service, Veterans Affairs San Diego Healthcare System, 3350 La Jolla Village Drive, San Diego, CA, USA

[3] Shu Chien-Gene Lay Department of Bioengineering, University of California San Diego, La Jolla, CA, USA

(UTE-qMT) readout sequence has enabled the application of qMT analysis to measure the macromolecular fraction (MMF) of cortical bones [18–20]. Other qMT parameters such as magnetization exchange rates between the free water and macromolecular pools may also provide insights into the quality of the bone that accounts for fracture risk [21, 22].

Yet, even with the use of UTE readouts, it is unclear whether the signal-to-noise ratios (SNR) of bone MT-weighted images is sufficient for qMT modeling. From previous MT studies on other tissues, it is known that the measurements of exchange rates are highly affected by the SNR of the images, and to a much greater degree than the MMF measurements are [23, 24]. Such SNR-based reliability of qMT modeling has not been studied for UTE-qMT imaging of bones. Towards the goal of developing qMT parameters as robust imaging markers that are correlated to bone fracture risk, a systematic assessment of the robustness and reliability of bone UTE-qMT must be performed (including the minimum SNR requirements) and strategies must be established for improving qMT parameter measurements.

In this study, we built a digital phantom through UTE-qMT simulation that mimics the MR properties of cortical bones. Unlike in vivo or ex vivo qMT studies, the simulation-based approach allows one to examine whether the qMT fitting is robust and reliable as the ground truths are known. Multiple series of MT-weighted images were synthesized to generate a wide range of SNR levels to examine the effect of SNR on qMT fitting results. The number of data points and the initial points for the qMT fitting were controlled to simulate how acquisition and analysis pipelines can affect the qMT fitting result. An ex vivo rat leg bone was scanned to validate the digital phantom results. For both digital phantom and ex vivo data, a tensor-based multidimensional denoising algorithm [25] was tested as a potential solution for the inherently low SNR of bone MRI and compared its performance with conventional Gaussian filtering.

Materials and methods

Digital phantom preparation

Digital phantom preparation was performed using custom-written MATLAB code (MathWorks, Natick, MA). The overall flow of phantom preparation and analysis is summarized in Fig. 1.

The binary spin bath (BSB) model was assumed for the digital phantom generation, modeling the cortical bone as a combination of two compartments, the free water pool (pool *a*) and the macromolecular pool (pool *b*) [26]. The BSB model with a pulsed saturation scheme can be well

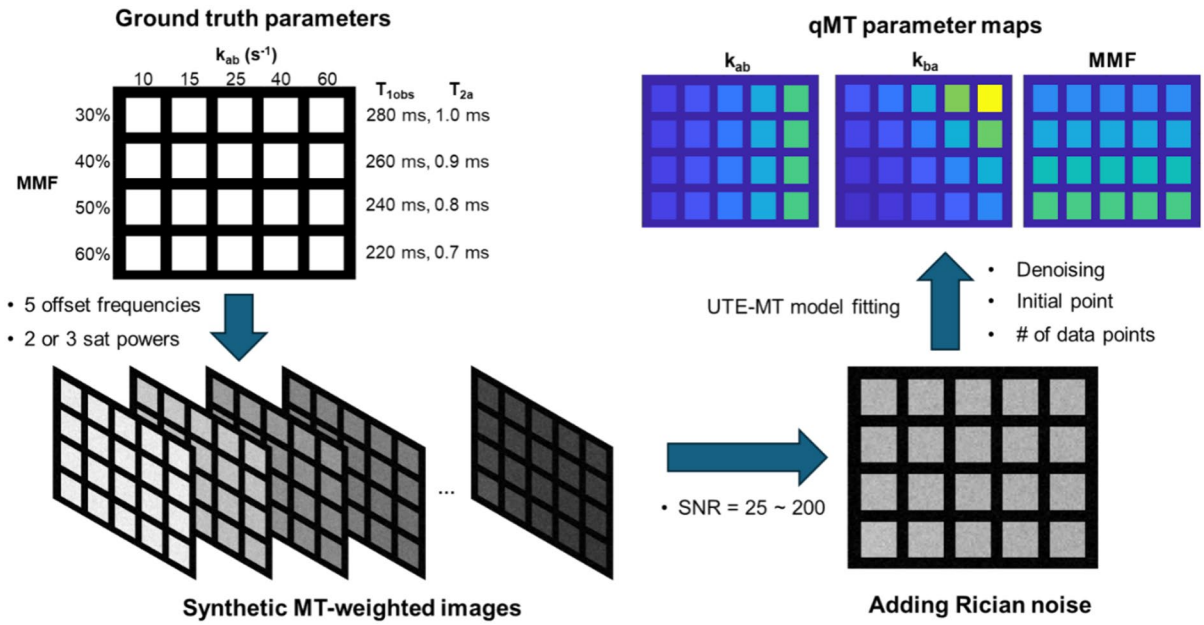

Fig. 1 Schematic flow of digital phantom preparation and qMT fitting. Twenty digital cortical bone chip images acquired at two or three saturation powers and five offset frequencies are simulated based on the UTE-qMT parameters measured from previous cortical bone studies. The Rician noise is added to the simulated bone chip images to generate the range of SNR levels from 25 to 200. The simulated bone chip images with added noise are fitted back to the UTE-qMT model to measure the macromolecular fraction (MMF) and exchange rates (k_{ab} and k_{ba}) by testing a different number of data points, selection of initial points of nonlinear fitting and applying a denoising algorithm

described by the rectangular pulse (RP) model by Sled and Pike [27], which was further modified for multiple acquisitions after a single MT preparation pulse [21]. This modified RP model was used for both generating digital phantoms and subsequent fitting for testing different SNR levels, the number of data points, and the effect of initial points for nonlinear fitting.

The modified RP model is described by a total of seven parameters: The size of the free water pool (M_{0a}), longitudinal relaxation rates of the free water and macromolecular pool (R_{1a} and R_{1b}), exchange rate from free water to macromolecular pool (k_{ab}), MMF (defined as $M_{0b}/(M_{0a}+M_{0b})$), T_2 of free water and macromolecular pools (T_{2a} and T_{2b}). As shown in previous studies, R_{1b} can be fixed to 1 s^{-1} [26, 28–30]. R_{1a} can be determined by other parameters and observed T_1 (e.g., $T_{1obs}=1/R_{1obs}$):

$$R_{1a} = R_{1obs} - \frac{k_{ab}(R_{1b} - R_{1obs})}{R_{1b} - R_{1obs} + \frac{k_{ab}(1-MMF)}{MMF}}$$

Thus, with the R_{1obs} measured, a total of five parameters can be determined through fitting. The exchange rate from the macromolecular pool to the free water pool (k_{ba}) can be determined as $k_{ab}\frac{1-MMF}{MMF}$

The input qMT parameters for generating digital phantoms were chosen from previous studies on UTE-qMT imaging of cortical bones [21, 31] (MMF = 30–60%, k_{ab} = 10–60 s^{-1}, T_{1obs} = 220–280 ms, T_{2a} = 0.7–1.0 ms, T_{2b} = fixed to 15 μs [32]). Twenty combinations of these parameters were used for simulating different conditions of cortical bones. For each condition, 324 qMT spectra were simulated to create a digital bone chip with the size of 18 × 18 voxels. Three MT saturation powers (3SP, flip angle = 400°, 800°, 1200°) and five offset frequencies (2, 5, 10, 20, 50 kHz) were used to generate qMT spectra. To simulate different levels of SNR, Rician noise with zero mean and different levels of standard deviation were added to the images so that the SNR of the image at the lowest saturation power (400°) and the largest offset frequency (50 kHz) ranges from 25 to 200. SNR was calculated as the mean signal intensity of digital phantoms divided by the standard deviation of the Rician noise used for noise generation. All the SNRs reported in this study are based on the image simulated or acquired at the lowest saturation power and the largest offset frequency unless indicated otherwise.

Digital phantom analysis

The prepared digital phantom images were fitted back into the UTE-qMT model to quantify the MMF and exchange rates (k_{ab} and k_{ba}) and observe whether the results matched the input parameters used for generating the phantoms. The non-linear fitting was performed using the 'lsqcurvefit' function in MATLAB with the default Trust-region fitting algorithm.

To assess the effect of the number of saturation powers and offset frequencies, we tested the full set of MT spectra (3 saturation powers and 5 offset frequencies, 15 data points) and the MT spectra with only 2 saturation powers (2SP, 800° dataset excluded, 10 data points). For this assessment, the initial point of non-linear fitting was fixed to the ground truth of each phantom so that only the effect of the number of data points can be assessed. The effect of the initial point of the nonlinear fitting process was also tested by using the initial point of either the ground truth of each phantom or the fixed one (MMF = 50%, k_{ab} = 25 s^{-1}, T_{1obs} = 240 ms, T_{2a} = 0.8 ms), near the midpoint of the range of parameters tested. All these assessments were done at different SNR levels.

A denoising algorithm was tested on the digital phantoms to examine whether qMT parameter fitting results improved. Among numerous potential algorithms, we tested a recently developed tensor Marchenko-Pastur distribution Principal Component Analysis (tMPPCA) method [25]. The digital phantom image with the SNR of 50 was denoised by tMPPCA with a window size of 3 × 3 × 3 [33]. The Gaussian filtering with the kernel standard deviation fixed to 1 was also tested for comparison.

Ex vivo *rat bone MR image acquisition and analysis*

An ex vivo rat leg bone was scanned on a 3 T scanner (Bruker, Billerica, MA) with a 1 cm loop coil to confirm the digital phantom results. The bone marrow of the bone was removed and placed in Fomblin (Ausimont, Thorofare, NJ) for susceptibility-matching purposes. MT-weighted UTE images were acquired at three saturation powers (500°, 1000°, 1500°) and five offset frequencies (2, 5, 10, 20, 50, kHz). Readout parameters are as follows: TR/TE = 86/0.026 ms, number of spokes per MT saturation = 13, inter-spoke TR = 5 ms, flip angle = 10°, field-of-view (FOV) = 10 mm × 10 mm × 80 mm, matrix = 84 × 84 × 84, receiver bandwidth = 100 kHz. The MT-weighted image acquisition was repeated 64 times to manually control the number of averages (NA). NA of 1, 4, 8, 16, 32, and 64 were tested to match with the SNR of 25–200 used for digital phantom simulation. For the qMT fitting process, the T_{1obs} was assumed to be 250 ms [31, 34–38]. The effect of denoising on MT parameter fitting was also tested using the same tMPPCA denoising algorithm. All the analysis was performed twice, once with the full dataset (3SP) and once with 2 saturation powers (2SP, 1000° dataset excluded).

Results

Digital phantom simulation shows similar MMF fitting results from MT spectra with 2SP and 3SP datasets (Fig. 2A), whereas the exchange rate measurements are slightly improved on the 3SP dataset. The MMF measurement is relatively robust throughout the SNR levels tested ranging from 58.8 ± 27.4% (2SP) and 57.0 ± 25.7% (3SP) at SNR of 25 to 51.8 ± 6.3% (2SP) and 51.0 ± 5.1% (3SP) at SNR of 200 (Fig. 2B). The exchange rate measurements are unstable in the lower SNR levels and become comparable to the ground truth at the SNR of 150 or above. These trends are also shown in the parameter maps at different SNR levels shown in Fig. 2C.

Similar trends are seen from the assessment of the initial point effect (Fig. 3). Overall, the choice of initial points did not significantly affect the fitting results, while the MMF measurement is more stable than the exchange rate measurements (Fig. 3A). Exchange rate measurements are reliable at the SNR of 150 or above, regardless of the choice of the initial point for nonlinear fitting (Fig. 3B). Still, the MMF measurement shows that the initial point set to the ground truth gives a more accurate result than the fixed initial point for certain phantoms at high SNR levels. This better measurement of MMF is also translated to a marginally improved measurement of k_{ba} in certain phantoms (Fig. 3).

The improvement of qMT fitting via denoising was also observed (Fig. 4). Although following the patterns in the ground truth, the exchange rate maps are highly noisy due to the unstable fitting without denoising. Both tMPPCA and Gaussian denoising of the raw digital phantom images generate the parameter maps that are closer to the ground truths, albeit with some residual regional variations in the parameter maps. Interestingly, the tMPPCA algorithm showed a more accurate measurement of high MMF values than the Gaussian filtering.

To validate the digital phantom results, ex vivo rat bones were scanned, and the improvement of qMT fitting was observed along with increasing the number of averages (Fig. 5). The SNR of raw images (saturation power = 500°, offset frequency = 50 kHz) increased from 37.4 (NA = 1) to 306.4 (NA = 64), matching with the SNR levels tested in the digital phantom simulations. Denoising via the tMPPCA method was tested on the NA = 1 dataset, which showed substantial improvement of SNR (131.6) and the subsequent qMT fitting that generated a result comparable to the one from the NA = 64 dataset with preserved spatial resolution (Fig. 5). The Gaussian filtering also showed improvement

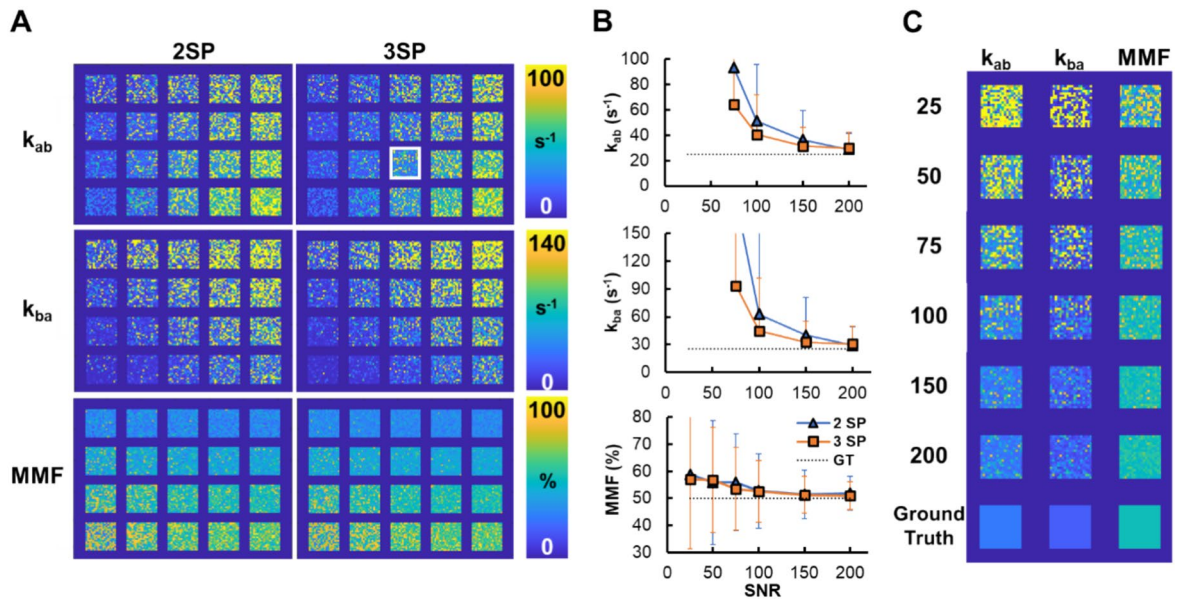

Fig. 2 The effect of the number of data points and signal-to-noise ratio (SNR) on cortical bone UTE-qMT fitting. The UTE-qMT parameters acquired via fitting 2 saturation powers (400° and 1200°, 2SP) and 3 saturation powers (400°, 800° and 1200°, 3SP) are compared. **A** UTE-qMT parameter maps generated from the dataset with SNR of 100 with the initial point chosen as the ground truth of each phantom. **B** The exchange rates (k_{ab} and k_{ab}) show the fitting results are more stable and closer to the ground truth upon using the 3SP dataset. Macromolecular fraction (MMF) measurements are stable for both 2SP and 3SP datasets. The 2SP dataset shows higher spatial variation of parameter fitting represented as larger standard deviations of the measurements. The measurements are from the phantom with the white box shown in A. k_{ab} and k_{ba} measurements are only shown at SNR of 75 or above due to abnormally large values from unstable fitting. **C** UTE-qMT parameters maps of the phantom analyzed (white box in A) at different SNR levels (25–200) and the maps of ground truth parameters

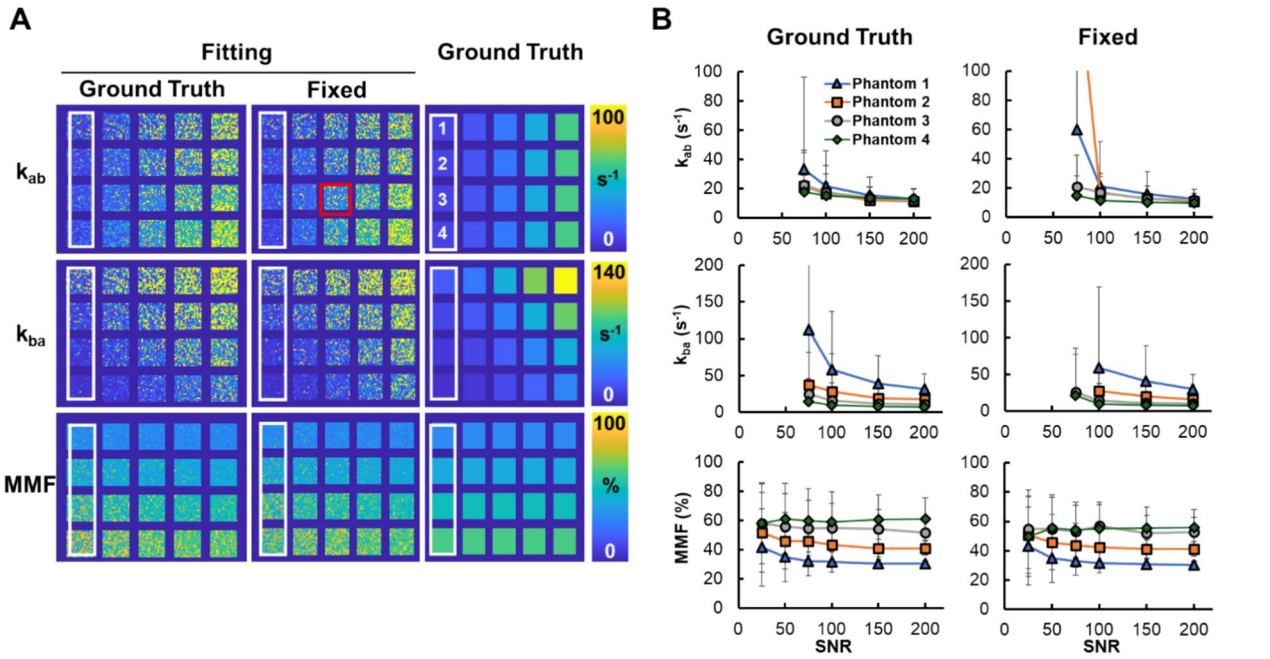

Fig. 3 The effect of the choice of initial point of nonlinear fitting of the UTE-qMT model. **A** UTE-qMT parameter maps from digital phantoms with three saturation powers and an SNR of 100. Parameter maps in the first two columns (Fitting) are the fitting results from using the initial point of either the ground truth of each phantom (Ground Truth) or the fixed values (parameters used for the phantom with the red box; Fixed). Ground truth maps are also included in the right-most column for comparison. **B** The macromolecular fraction (MMF) and exchange rate (k_{ab} and k_{ba}) measurements from 4 phantoms indicated in the white boxes shown in A. k_{ab} and k_{ba} measurements are only shown at SNR of 75 or above due to abnormally large values from unstable fitting

in parameter fitting, but substantial spatial blurring is also observed as expected.

The quantitative measurements of qMT parameters from ex vivo scans also show the robust measurement MMF across all NAs tested, whereas the exchange rate measurements are not reliable at NA of 1 (Fig. 6). Compared to digital phantoms, however, low SNR ex vivo scans (NA = 1, 4, 8) show much more comparable results to those from high SNR scans (NA = 32 and 64). The tMPPCA denoising of the dataset with NA of 1 substantially improved the quality of fitting compared to the original image. Despite the overestimated MMF (43.4 ± 7.2 vs. 40.4 ± 5.2%; Fig. 6A) and underestimated exchange rates (k_{ab}: 20.7 ± 12.8 s^{-1} vs. 22.6 ± 9.1; k_{ba}: 28.2 ± 21.2 s^{-1} vs 34.2 ± 18.6 s^{-1}; Fig. 6B, C), the results from the denoised NA = 1 dataset are comparable to those from the NA = 64 dataset. The use of the 3SP dataset significantly reduced the variation of all the UTE-qMT parameter measurements in the given ROI compared to the results from the 2SP dataset.

Discussion

Here, we systematically assessed the SNR requirements and how the fitting process affects the UTE-qMT imaging of bone. Similar to qMT imaging of other tissues, the MMF measurement was robust across a range of SNR levels, whereas exchange rate measurements became accurate when the SNR reached around 150 or above. The UTE-qMT fitting process also turned out to be robust against the selection of the initial point of the nonlinear fitting process, and the 2SP dataset generated comparable results as those from 3SP datasets. The denoising algorithm tested in this study substantially improved the fitting accuracy. These results were also reproduced in ex vivo rat leg bone scans, with relatively more robust MMF measurements and substantial improvement of qMT measurements after denoising.

The advantage of the digital phantom approach demonstrated in this study is the known ground truth. Although the quality of qMT fitting is usually measured by the goodness-of-fit, whether the ground truth value is obtained through the fitting cannot be known by actual scans, unless followed by validation studies such as histology or biochemical assays from tissue samples. By knowing the ground truth values, the digital phantom simulation approach allows examining whether the qMT fitting provides correct results and permits subsequent optimization of the data acquisition and analysis pipeline. Optimizing the qMT fitting pipeline using the known ground truth is also expected to facilitate the development of more advanced techniques for qMT fitting such as neural network-based approaches by

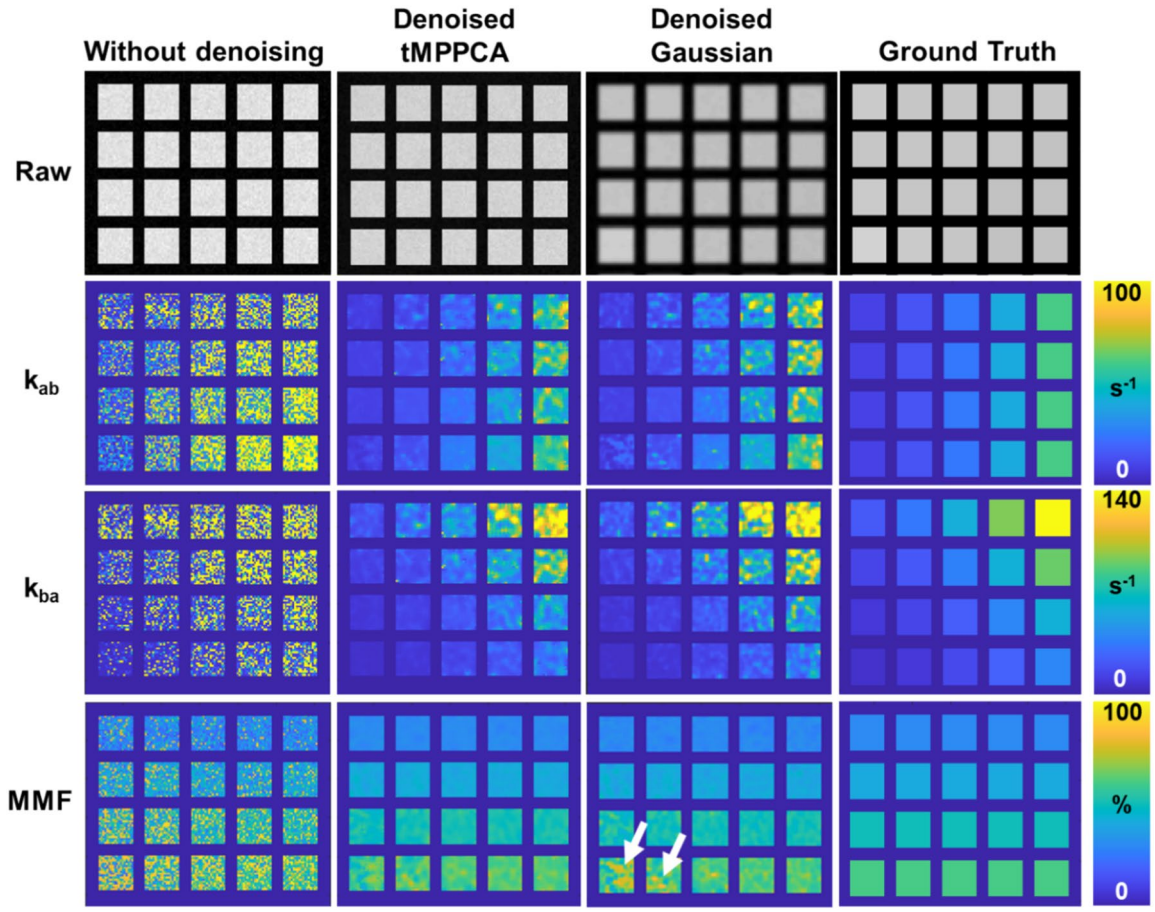

Fig. 4 tMPPCA denoising improves the UTE-qMT fitting of simulated digital phantoms. The simulated digital phantom with three saturation powers and an SNR of 50 was tested. The initial point of fitting was selected as the ground truth of each phantom. Both tMPPCA and Gaussian denoising have significantly improved the UTE-qMT parameter fitting with less noise in the parameter map, and the results are more comparable to the ground truth. The white arrows indicate the difference in MMF measurement between tMPPCA and Gaussian denoising

providing more accurate and refined training datasets [39, 40].

Comparing the fitting results with the ground truth showed that the exchange rate measurements are highly SNR dependent whereas MMF measurements are more robust even in the low SNR regime, regardless of the number of data points and initial points tested. The unstable fitting of exchange rates at low SNR has been previously shown from qMT studies on other soft tissues [23, 41]. The qMT study on human patellar cartilage reported that the percentage change of the exchange rate becomes lower than 1% only after the SNR of an image becomes 75 or higher [23]. Our digital phantom-based analysis shows that at least an SNR of 100–150 is needed for reasonable voxel-based measurements of exchange rates, whereas MMF measurements are acceptable even with an SNR of around 50. The unstable fitting of exchange rates at SNR of 50 or lower generated unrealistically large values ($k_{ab} > 10^3$ and $k_{ba} > 5 \times 10^3$ s^{-1}) and variations that had to be excluded from the measurements (Figs. 2B and 3B). The instability of exchange rate measurements may be alleviated by setting up narrower but still realistic boundary conditions during the fitting process. Still, considering the inherently low SNR of actual bone MR images acquired in a clinically feasible scan time, only a region-of-interest (ROI)-based analysis seems applicable for the exchange rate measurements unless certain strategies to improve the SNR are employed, such as low-pass filtering and other denoising algorithms.

As a potential method of improving the SNR and corresponding qMT fitting results, we tested the tMPPCA algorithm on both digital phantoms and rat bone data and compared it with conventional Gaussian filtering. The tMPPCA is designed for denoising multidimensional MRI data by leveraging the redundancy in the extra dimensions [25]. This algorithm has demonstrated substantial improvement of SNR of multi-echo images, diffusion-weighted images, and T_1-weighted images, as well as subsequent parameter fitting results [25, 33]. We

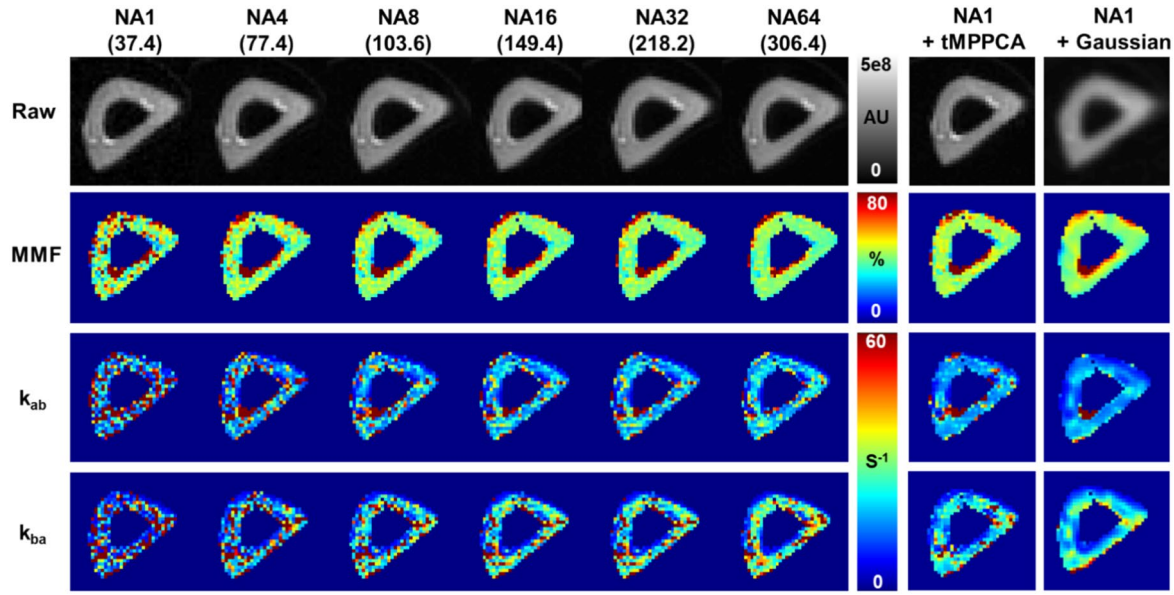

Fig. 5 Ex vivo rat leg bone scans with different degrees of averaging. The number of averages (NA) was controlled from 1 to 64 to cover the SNR range of 25–200 simulated for digital phantoms. The SNR levels are indicated in parentheses. Denoising via the tMPPCA algorithm and Gaussian filter were also tested on the NA1 dataset (NA1 + dn). The macromolecular fraction (MMF) fitting is stable except for the one from the NA1 dataset, whereas the exchange rate maps (k_{ab} and k_{ba}) are steadily improving with the increasing NA. The tMPPCA-denoised NA1 dataset shows comparable results with the NA32 and NA64 datasets. The denoising with the Gaussian filter also shows improved exchange rate measurement along with a significant blurring in both raw image and parametric maps. The UTE-qMT parameter maps shown here are generated using the full dataset acquired (three saturation powers)

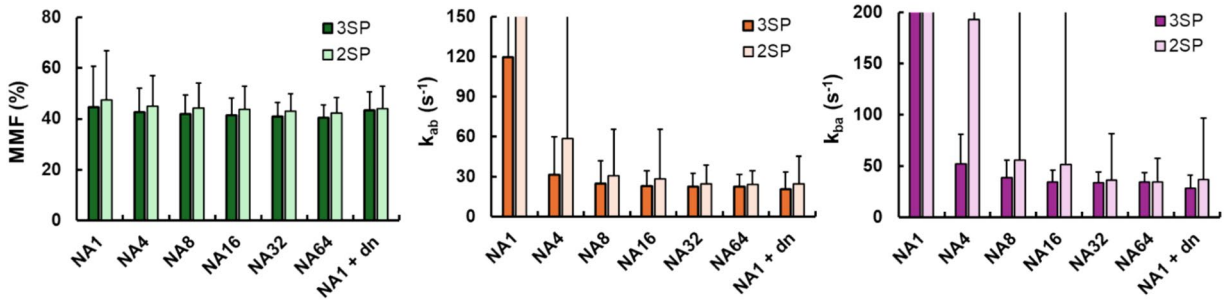

Fig. 6 Ex vivo rat bone scan measurements. The UTE-qMT fitting results shown in Fig. 5 were measured with a region of interest covering the entire rat bone. Macromolecular fraction (MMF) measurements show stable measurements across the range of number of averages (NA) used, regardless of using 2 saturation powers (2SP) and 3 saturation powers (3SP). The measurement of exchange rates (k_{ab} and k_{ba}) is more NA-dependent than MMF measurements. The variation of exchange rate measurements is also significantly reduced when using the 3SP dataset. Due to significant spatial blurring upon Gaussian denoising, only the results from tMPPCA denoising (NA1 + dn) are shown

hypothesized that this algorithm would also bring high SNR gain to qMT datasets as qMT data are inherently multidimensional due to repeated acquisitions at different saturation powers and offset frequencies. The digital phantom simulation showed that tMPPCA denoising enables accurate voxel-wise measurement of exchange rates even with an SNR of 50, similar to the results from Gaussian filtering. This result was validated by applying the same algorithm to the rat bone dataset, shown by the similar fitting results between the raw high SNR dataset (NA = 64) and the denoised low SNR dataset (NA = 1). Compared to Gaussian filtering, the tMPPCA denoising did not show any spatial blurring. These results indicate that even with the low SNR raw data, the exchange rates can also be reliably measured with a proper denoising strategy.

While MMF alone can be a great imaging marker of the content of organic matrix in the bone, exchange rates can also be valuable markers of macromolecule conditions in the bone. With the growing evidence that BMD is not sufficient to examine the bone fracture risk, bone quality is drawing

more attention as another determinant of bone fracture risk [42–44]. For instance, non-enzymatic crosslinking of collagen fibrils via advanced glycation end products in the cortical bone is considered to be a key contributor to the increased fracture risk in type 2 diabetes patients despite the preserved or even elevated BMD measurements [45–47]. Since the exchange rate measurements were demonstrated to be altered upon crosslinking collagens in cornea and cartilage, as well as other polymers [48–50], robust measurements of exchange rates via UTE-qMT modeling can potentially be a valuable marker of assessing the bone quality and fracture risk.

A typical limitation of qMT parameter measurements via the BSB model is parameter correlation. Previous studies have shown that MMF and k_{ab} measurements can be coupled, rather than independent [24, 51]. This parameter coupling was also observed in this study, as shown in the scatter plot of voxel-wise measurement of MMF and k_{ab} (Figure S1). An anisotropic distribution of MMF and k_{ab} measurements was observed throughout the SNR levels tested, indicating that these parameter measurements are not independent. The overall trend of MMF and k_{ab} measurement shows the tendency to compensate for the underestimation of MMF with the overestimation of k_{ab} and vice versa, which is a previously reported phenomenon [27]. Other qMT parameter estimation approaches that do not depend on nonlinear fitting, such as the dictionary-matching method [52], may alleviate the issue.

In this study, we only tested the effect of SNR, the number of data points, and the selection of initial points for the fitting, but other parameters involved in the image acquisition and analysis procedure can also be tested using the digital phantom approach in the future. The number and selection of offset frequencies and saturation powers can be further tested to identify the combination of these parameters that gives the best fitting accuracy with the minimum data acquisition to reduce the scan time. Testing for the effect of B_1 inhomogeneity and T_1 relaxation time is another validation test that may be performed through digital phantoms. In this study, we assumed a perfect B_1 homogeneity and T_1 relaxation time measurement. For in vivo UTE-qMT scans of cortical bone, however, the accurate measurements of B_1 inhomogeneity and T_1 relaxation are challenging due to the short T_2* of the cortical bone [34]. Examining the tolerance of B_1 and T_1 errors during the qMT fitting will give a better assessment of the reliability of the UTE-qMT imaging. In that regard, the ex vivo rat bone scan results can be improved with the actual measurement of B_1 inhomogeneity and T_1. These studies should also be validated through in vivo scans in the future. Due to the higher body temperature and other tissues surrounding the cortical bone (e.g., bone marrow and muscle), the SNR of in vivo bone scan is expected to be lower than the ex vivo scans [53]. The digital phantom approach taken in this study may also be biased due to the discrepancy between the in vivo conditions and the model chosen for generating digital phantoms and subsequent fitting. Whether the findings through the digital phantom demonstrated in this study can be applied to in vivo scans should be further examined. Finally, we chose the tMPPCA algorithm with a fixed window size for denoising. Other denoising algorithms, as well as image filtering and ROI-averaging with different numbers of voxels within an ROI, can also be tested for establishing a robust UTE-qMT analysis pipeline.

Conclusion

Here, we demonstrated the usage of digital phantom simulation to assess the reliability of qMT measurements. Similar to qMT imaging of other tissues, cortical bone digital phantoms showed robust MMF measurements whereas exchange rate measurements were unstable in low SNR levels. The number of data points and the selection of initial points tested in this study yielded negligible effects on the UTE-qMT fitting results. Denoising via the tMPPCA method showed substantial improvement in qMT fitting in both simulation and ex vivo scans, supporting the feasibility of reliable voxel-wise measurements of bone UTE-qMT parameters.

Supplementary Information The online version contains supplementary material available at https://doi.org/10.1007/s10334-024-01190-7.

Acknowledgements The authors acknowledge grant support from the Veterans Affairs Research and Development Services (Merit Awards I01BX005952, I01CX001388, and I01CX002211); National Institutes of Health (R01AR068987, R01AR079484, RF1AG075717, and K01AR080257); and University of California San Diego (RG114138).

Author contributions Conceptualization, S.S. and E.Y.C; Methodology, S.S., D.M, Q.T..; Software, S.S.; Validation, S.S., S.J., Y.M, J.D., and E.Y.C.; Formal Analysis, S.S.; Investigation, S.S.; Resources, D.M., Q.T., E.Y.C.; Data Curation, S.S.; Writing–Original Draft Preparation, S.S.; Writing–Review and Editing, S.S., E.Y.C.; Visualization, S.S; Supervision, S.J., Y.M., J.D., E.Y.C.; Funding Acquisition, S.S., S.J., Y.M., J.D., E.Y.C.

Data availability The data supporting the reported findings and the code used for analyzing the data are available from the corresponding authors upon reasonable request.

Declarations

Conflict of interest There are no conflicts of interest to disclose.

Ethical standard All experimental procedures are in accordance with the ethical standards of the institutional research committee.

References

1. Wu AM, Bisignano C, James SL et al (2021) Global, regional, and national burden of bone fractures in 204 countries and territories, 1990–2019: a systematic analysis from the Global Burden of Disease Study 2019. Lancet Healthy Longev 2(9):e580–e592. https://doi.org/10.1016/S2666-7568(21)00172-0
2. Xiao PL, Cui AY, Hsu CJ et al (2022) Global, regional prevalence, and risk factors of osteoporosis according to the World Health Organization diagnostic criteria: a systematic review and meta-analysis. Osteoporos Int 33(10):2137–2153. https://doi.org/10.1007/s00198-022-06454-3
3. Sun H, Saeedi P, Karuranga S et al (2022) IDF Diabetes Atlas: Global, regional and country-level diabetes prevalence estimates for 2021 and projections for 2045. Diabetes Res Clin Pract 183:109119. https://doi.org/10.1016/j.diabres.2021.109119
4. Schuit SCE, Van Der Klift M, Weel AEAM et al (2004) Fracture incidence and association with bone mineral density in elderly men and women: the Rotterdam Study. Bone 34(1):195–202. https://doi.org/10.1016/j.bone.2003.10.001
5. De Laet CEDH, Van Hout BA, Burger H, Hofman A, Pols HAP (1997) Bone density and risk of hip fracture in men and women: cross sectional analysis. BMJ 315(7102):221–225. https://doi.org/10.1136/bmj.315.7102.221
6. Trémollieres FA, Pouillès JM, Drewniak N, Laparra J, Ribot CA, Dargent-Molina P (2010) Fracture risk prediction using BMD and clinical risk factors in early postmenopausal women: sensitivity of the WHO FRAX tool. J Bone Miner Res 25(5):1002–1009. https://doi.org/10.1002/jbmr.12
7. Lorentzon M (2020) The importance and possible clinical impact of measuring trabecular and cortical bone microstructure to improve fracture risk prediction. J Bone Miner Res 35(5):831–832. https://doi.org/10.1002/jbmr.3940
8. Burr DB (2002) The contribution of the organic matrix to bone's material properties. Bone 31(1):8–11. https://doi.org/10.1016/S8756-3282(02)00815-3
9. Unal M, Creecy A, Nyman JS (2018) The role of matrix composition in the mechanical behavior of bone. Curr Osteoporos Rep 16(3):205–215. https://doi.org/10.1007/s11914-018-0433-0
10. Sled JG, Pike GB (2001) Quantitative imaging of magnetization transfer exchange and relaxation properties in vivo using MRI. Magn Reson Med 46(5):923–931. https://doi.org/10.1002/mrm.1278
11. Henkelman RM, Stanisz GJ, Graham SJ (2001) Magnetization transfer in MRI: a review. NMR Biomed 14(2):57–64. https://doi.org/10.1002/nbm.683
12. Ramani A, Dalton C, Miller DH, Tofts PS, Barker GJ (2002) Precise estimate of fundamental in-vivo MT parameters in human brain in clinically feasible times. Magn Reson Imaging 20(10):721–731. https://doi.org/10.1016/S0730-725X(02)00598-2
13. Wu T, Byun NE, Wang F et al (2020) Longitudinal assessment of recovery after spinal cord injury with behavioral measures and diffusion, quantitative magnetization transfer and functional magnetic resonance imaging. NMR Biomed 33(4):e4216. https://doi.org/10.1002/nbm.4216
14. Bryant ND, Li K, Does MD et al (2014) Multi-parametric MRI characterization of inflammation in murine skeletal muscle. NMR Biomed 27(6):716–725
15. Shin SH, Wendland MF, Wang J, Velasquez M, Vandsburger MH (2023) Noninvasively differentiating acute and chronic nephropathies via multiparametric urea-CEST, nuclear Overhauser enhancement -CEST, and quantitative magnetization transfer MRI. Magn Reson Med 89(2):774–786. https://doi.org/10.1002/mrm.29477
16. Jang A, Han PK, Ma C et al (2023) B 1 inhomogeneity-corrected T1 mapping and quantitative magnetization transfer imaging via simultaneously estimating B loch-S iegert shift and magnetization transfer effects. Magn Reson Med 90(5):1859–1873
17. Janve VA, Zu Z, Yao SY et al (2013) The radial diffusivity and magnetization transfer pool size ratio are sensitive markers for demyelination in a rat model of type III multiple sclerosis (MS) lesions. Neuroimage 74:298–305. https://doi.org/10.1016/j.neuroimage.2013.02.034
18. Ma Y, Shao H, Du J, Chang EY (2016) Ultrashort echo time magnetization transfer (UTE-MT) imaging and modeling: magic angle independent biomarkers of tissue properties. NMR Biomed 29(11):1546–1552. https://doi.org/10.1002/nbm.3609
19. Ma YJ, Jerban S, Jang H, Chang D, Chang EY, Du J (2020) Quantitative Ultrashort Echo Time (UTE) magnetic resonance imaging of bone: an update. Front Endocrinol 11:567417. https://doi.org/10.3389/fendo.2020.567417
20. Chang EY, Du J, Chung CB (2015) UTE imaging in the musculoskeletal system: UTE Imaging in the MSK System. J Magn Reson Imaging 41(4):870–883. https://doi.org/10.1002/jmri.24713
21. Ma YJ, Chang EY, Carl M, Du J (2018) Quantitative magnetization transfer ultrashort echo time imaging using a time-efficient 3D multispoke Cones sequence: 3D Multispoke UTE-Cones-MT Imaging. Magn Reson Med 79(2):692–700. https://doi.org/10.1002/mrm.26716
22. Ma Y, Tadros A, Du J, Chang EY (2018) Quantitative two-dimensional ultrashort echo time magnetization transfer (2D UTE-MT) imaging of cortical bone. Magn Reson Med 79(4):1941–1949. https://doi.org/10.1002/mrm.26846
23. Sritanyaratana N, Samsonov A, Mossahebi P, Wilson JJ, Block WF, Kijowski R (2014) Cross-relaxation imaging of human patellar cartilage in vivo at 3.0T. Osteoarthritis Cartilage 22(10):1568–1576. https://doi.org/10.1016/j.joca.2014.06.004
24. Portnoy S, Stanisz GJ (2007) Modeling pulsed magnetization transfer. Magn Reson Med 58(1):144–155. https://doi.org/10.1002/mrm.21244
25. Olesen JL, Ianus A, Østergaard L, Shemesh N, Jespersen SN (2023) Tensor denoising of multidimensional MRI data. Magn Reson Med 89(3):1160–1172. https://doi.org/10.1002/mrm.29478
26. Henkelman RM, Huang X, Xiang QS, Stanisz GJ, Swanson SD, Bronskill MJ (1993) Quantitative interpretation of magnetization transfer. Magn Reson Med 29(6):759–766. https://doi.org/10.1002/mrm.1910290607
27. Sled JG, Pike GB (2000) Quantitative interpretation of magnetization transfer in spoiled gradient echo MRI sequences. J Magn Reson 145(1):24–36. https://doi.org/10.1006/jmre.2000.2059
28. Teixeira AGRP, Malik SJ, Hajnal JV (2019) Fast quantitative MRI using controlled saturation magnetization transfer. Magn Reson Med 81(2):907–920. https://doi.org/10.1002/mrm.27442

29. Rowley CD, Nelson MC, Campbell JSW, Leppert IR, Pike GB, Tardif CL (2024) Fast magnetization transfer saturation imaging of the brain using MP2RAGE T1 mapping. Magn Reson Med. https://doi.org/10.1002/mrm.30143
30. Marschner H, Pampel A, Müller R et al (2023) High-resolution magnetization-transfer imaging of *post-mortem* marmoset brain: comparisons with relaxometry and histology. Neuroimage 268:119860. https://doi.org/10.1016/j.neuroimage.2023.119860
31. Jerban S, Ma Y, Wan L et al (2019) Collagen proton fraction from ultrashort echo time magnetization transfer (UTE-MT) MRI modelling correlates significantly with cortical bone porosity measured with micro-computed tomography (μCT). NMR Biomed 32(2):e4045
32. Chan RW, Myrehaug S, Stanisz GJ, Sahgal A, Lau AZ (2019) Quantification of pulsed saturation transfer at 1.5 T and 3T. Magn Reson Med. 82(5):1684–1699
33. Herthum H, Hetzer S (2024) Tensor denoising of quantitative multi-parameter mapping. Magn Reson Med. 92(1):145–157
34. Ma YJ, Lu X, Carl M et al (2018) Accurate T_1 mapping of short T_2 tissues using a three-dimensional ultrashort echo time cones actual flip angle imaging-variable repetition time (3D UTE-Cones AFI-VTR) method: Accurate T_1 Mapping With 3D UTE-Cones AFI-VTR. Magn Reson Med 80(2):598–608. https://doi.org/10.1002/mrm.27066
35. Chen J, Chang EY, Carl M et al (2017) Measurement of bound and pore water T1 relaxation times in cortical bone using three-dimensional ultrashort echo time cones sequences. Magn Reson Med 77(6):2136–2145. https://doi.org/10.1002/mrm.26292
36. Techawiboonwong A, Song HK, Leonard MB, Wehrli FW (2008) Cortical bone water in vivo quantification with ultrashort echo-time MR imaging. Radiology 248(3):824–833. https://doi.org/10.1148/radiol.2482071995
37. Rad HS, Lam SCB, Magland JF et al (2011) Quantifying cortical bone water in vivo by three-dimensional ultra-short echo-time MRI. NMR Biomed 24(7):855–864. https://doi.org/10.1002/nbm.1631
38. Chen J, Grogan SP, Shao H et al (2015) Evaluation of bound and pore water in cortical bone using ultrashort-TE MRI. NMR Biomed 28(12):1754–1762. https://doi.org/10.1002/nbm.3436
39. Luu HM, Kim D, Kim J, Choi S, Park S (2021) qMTNet: accelerated quantitative magnetization transfer imaging with artificial neural networks. Magn Reson Med 85(1):298–308. https://doi.org/10.1002/mrm.28411
40. Luu HM, Park SH (2023) SIMPLEX: Multiple phase-cycled bSSFP quantitative magnetization transfer imaging with physic-guided simulation learning of neural network. Neuroimage 284:120449. https://doi.org/10.1016/j.neuroimage.2023.120449
41. Yarnykh VL (2012) Fast macromolecular proton fraction mapping from a single off-resonance magnetization transfer measurement. Magn Reson Med 68(1):166–178. https://doi.org/10.1002/mrm.23224
42. Fonseca H, Moreira-Gonçalves D, Coriolano HJA, Duarte JA (2014) Bone quality: the determinants of bone strength and fragility. Sports Med 44(1):37–53. https://doi.org/10.1007/s40279-013-0100-7
43. Bouxsein ML (2003) Bone quality: where do we go from here? Osteoporos Int 14:118–127. https://doi.org/10.1007/s00198-003-1489-x
44. Link TM, Kazakia G (2020) Update on imaging-based measurement of bone mineral density and quality. Curr Rheumatol Rep 22(5):13. https://doi.org/10.1007/s11926-020-00892-w
45. Saito M, Marumo K (2010) Collagen cross-links as a determinant of bone quality: a possible explanation for bone fragility in aging, osteoporosis, and diabetes mellitus. Osteoporos Int 21(2):195–214. https://doi.org/10.1007/s00198-009-1066-z
46. Hofbauer LC, Busse B, Eastell R et al (2022) Bone fragility in diabetes: novel concepts and clinical implications. Lancet Diabetes Endocrinol 10(3):207–220. https://doi.org/10.1016/S2213-8587(21)00347-8
47. Khosla S, Samakkarnthai P, Monroe DG, Farr JN (2021) Update on the pathogenesis and treatment of skeletal fragility in type 2 diabetes mellitus. Nat Rev Endocrinol 17(11):685–697. https://doi.org/10.1038/s41574-021-00555-5
48. Ho LC, Sigal IA, Jan NJ et al (2016) Non-invasive MRI assessments of tissue microstructures and macromolecules in the eye upon biomechanical or biochemical modulation. Sci Rep 6(1):32080. https://doi.org/10.1038/srep32080
49. Fishbein KW, Gluzband YA, Kaku M et al (2007) Effects of formalin fixation and collagen cross-linking on T2 and magnetization transfer in bovine nasal cartilage. Magn Reson Med 57(6):1000–1011
50. Gochberg DF, Fong PM, Gore JC (2001) Studies of magnetization transfer and relaxation in irradiated polymer gels - interpretation of MRI-based dosimetry. Phys Med Biol 46(3):799–811. https://doi.org/10.1088/0031-9155/46/3/314
51. Stanisz GJ, Kecojevic A, Bronskill MJ, Henkelman RM (1999) Characterizing white matter with magnetization transfer and T2. Magn Reson Med 42(6):1128–1136. https://doi.org/10.1002/(SICI)1522-2594(199912)42:6%3c1128::AID-MRM18%3e3.0.CO;2-9
52. Kim JW, Lee SL, Choi SH, Park SH (2019) Rapid framework for quantitative magnetization transfer imaging with interslice magnetization transfer and dictionary-driven fitting approaches. Magn Reson Med 82(5):1671–1683. https://doi.org/10.1002/mrm.27850
53. Han M, Rieke V, Scott SJ et al (2015) Quantifying temperature-dependent T1 changes in cortical bone using ultrashort echo-time MRI. Magn Reson Med 74(6):1548–1555